## PAPER

# Anapole-excited terahertz multifunctional spoof surface plasmon polariton directional Janus metastructures†

Hao Pan,[ab] Bing-xiang Li[*a] and Hai Feng Zhang ![ORCID] [*a]

The anapole mode, in which a distinct radiationless electromagnetic (EM) response in artificial media can be achieved, has attracted significant attention and been regarded as a promising candidate to initiate novel avenues to control the intrinsic radiative losses in nanophotonics and plasmonics, whose current research studies mainly focus on the manipulation of the one-directional incident wave. To exploit the propagation characteristic of incident waves in anapole-excited (AE) media, a set of terahertz (THz) multifunctional Janus metastructures (JMSs) for the opposite linear-polarized (LP) light excitation is presented in this paper. By introducing the directional-selective spoof surface plasmon polariton (SSPP) excited by anapole mode, a metastructure rasorber (MSR) possessing an absorption band of 2–3.08 THz (42.5%) and a co-polarized transmission window of 3.77–5.55 THz (38.2%) for the forward normal-incident LP wave is attained. Furthermore, the integration of the MSR and a polarization-conversation structure (PCS) can be used to fabricate a multifunctional Janus metadevice thus achieving the integration of EM energy harvesting, the co-polarized transmission, and cross-polarized reflection of light with opposite propagation directions, *i.e.*, an absorption band of 2.14–3.09 THz (36.3%) for the forward normal-incident LP wave, and a cross-polarized reflection band of 2.08–3.03 THz (37.2%) for the backward vertical-incident LP wave, while attaining an identical co-polarized transmission window of 3.95–5.2 THz (27.3%). Moreover, by utilizing the substantial field-localization properties of anapole modes supported by the nested opposite-directional SSPP with different sizes, the Janus metastructure absorber (JMA) can achieve non-overlapped absorption bands of 2.02–2.84 THz (33.7%) and 2.88–4.58 THz (45.6%) for the bidirectional normal-incident LP waves, respectively. A series of passive JMSs based on the anapole modes excited by the opposite-directional incident waves significantly extend the theoretical framework and application field of multipole electrodynamics, especially aimed at directional-selective management.

## 1. Introduction

Owing to the revolutionary developments in efficient, cost-effective, and reliable nanotechnologies based on optics, photonics is playing a more dominant role in the 21st century, for which noteworthy reaserch efforts have been made in multiple fields from chip manufacturing and modern pharmacology to astronomy and military depending on the power of light. Furthermore, the strategic and applicable requirements in futuristic nanotechnology will push photonics toward subwavelength

photonic integration and the control of energy efficiency, which can only be attained by employing the concepts of metastructures and metadevices based on an artificial homogeneous subwavelength configuration.[1–3] A broad spectrum of fundamental discoveries using metastructures have been achieved, *e.g.*, optical magnetism,[4,5] hyperbolic dispersion,[6,7] electromagnetically induced transmission,[8,9] arbitrary control of light's trajectories,[10,11] cloaking,[12,13] and epsilon-near-zero.[14,15] The intrinsic EM characteristics of metadevices to acquire these diverse functionalities mainly depend on controlling the properties of the amplitude, phase, operating frequency, polarization state, and spin angular momentum of the incident light.[16–20] Nevertheless, another characteristic of EM waves, namely the propagation direction (*i.e.*, *k* direction), is rarely exploited in the scenario of multifunctional metadevices and metaphotonics. A metastructure possessing different EM functionalities because of opposite incidence of waves resulting from breaking of the

[a] *College of Electronic and Optical Engineering & College of Flexible Electronics (Future Technology), Nanjing University of Posts and Telecommunications, Nanjing, 210023, China. E-mail: hanlor@163.com, bxli@njupt.edu.cn*

[b] *Department of Physics in College of Science, City University of Hong Kong, Hong Kong, Hong Kong*

This journal is © the Owner Societies 2023

*Phys. Chem. Chem. Phys.*, 2023, **25**, 11375–11386 | 11375

out-of-plane symmetry can be called the Janus metastructure (JMS) (Janus is the name of the two-faced God in Roman mythology[21]), which has received copious attention owing to its functional tunability and multifunctional integration.[22–26] Compared with nonreciprocal devices exhibiting time-reversal asymmetric transmission under an external bias (*e.g.*, static magnetic field[27,28]), nonlinear materials,[29] or time-varying components,[30,31] JMSs, as passive devices, can exhibit asymmetric but still reciprocal transmission only based on the traditional passive, linear, and low-loss materials instead of expensive, complicated and bulky equipment. Chen and his teammates proposed a passive JMS composed of cascaded anisotropic impedance sheets and different rotational-twist structures, thus enabling versatile functionalities including one-way anomalous refraction, one-way focusing, asymmetric focusing, and direction-controlled holograms.[23] Shang *et al.* demonstrated a Janus metastructure that can achieve different hologram functionalities in independent channels manipulated by the incident waves with different propagation.[26] Note that in the current JMSs manipulating the reflective or transmissive bidirectional waves by controlling their phase, amplitude, and polarization states to enable copious functionalities is mainly focused, but there is a lack of research on directional EM energy harvesting, which has great and promising potential for application in EM cloaking, solar battery, *etc.* In addition, the integration of more functions, *e.g.*, high-responsive communication, polarization-state control, *etc.*, while retaining the highly effective energy harvesting in one device can provide more selective diversity that is vital for compact integration devices in photonic communication.

Although there are copious conventional artificially tailored metastructures opening up the decisive aisles to fabricate highly responsive tools, the ever-increasing demand for more efficient and responsive metastructures has driven more efforts towards replacing these conventional nanostructures with more novel alternatives depending on their unique advantages. In 2007, Marinov *et al.*[32] introduced a novel optical metastructure relying on the third family of electrodynamics, namely the toroidal multipoles initially explored by Zel'dovich,[33] thus extending the uncharted territory of metamaterials. In particular, a toroidal dipole equivalent to the head-to-tail ring of magnetic dipoles attracts particular interest because of its strong field-localization capacity (ultra-high quality ($Q$) factor).[34,35] However, it is not until 2010 that Kaelberer and his researchers first experimentally observed the toroidal dipole response in a metastructure mainly consisting of the split-ring resonators across the microwave regime;[36] thus, extensive studies on metadevices driven by toroidal dipoles have been constantly carried out.[37–41] Furthermore, the destructive interference, originating from co-aligned toroidal and electric dipoles with identical angular momentum and parity properties which further produce the same radiation patterns, can yield an anapole mode under hidden far-field radiation and tightly squeezing EM fields,[42,43] which was also first experimentally discovered in the microwave range.[44] In light of the ability to localize the incident wave and support the high $Q$ resonance, well-engineered metastructures excited by anapole modes have emerged for copious subwavelength devices, *e.g.*, nonlinear harmonic signal sources,[45,46] cloaking devices,[47,48] sensitive sensors,[49–52] *etc.* However, the reported anapole modes supported by the corresponding metastructures are only excited by the single-directional incident EM wave to acquire the single functionality, thus leaving the directional features unexploited in previous works. Furthermore, it is still challenging and worthwhile to enable two-faced spacial asymmetric anapole excitation in a passive metastructure to achieve the different wave front manipulation upon opposite incidence, *i.e.*, one function for the incident wave propagating along one direction but a different function for the opposite direction illumination.

Here, we propose and demonstrate the THz $k$-dependent SSPP excited by copious anapole modes existing in the elliptic-ring metallic structures of different sizes, further analyzing the operation mechanism according to the physical investigation and theoretical simulation verification. Leveraging the nontrivial wave front-manipulation characteristic of direction-selective anapole modes supported by the SSPP, the multiple EM functionalities are combined into one JMS intrigued by opposite-directional incident waves, *i.e.*, the absorption-transmission rasorber for the forward normal-incident LP wave and the co-polarized reflection-transmission device for the backward normal-incident LP wave. Furthermore, to achieve the polarization-state manipulation of LP waves while attaining the energy harvesting, the JMS based on AE SSPP is combined with the metallic PCS, thus achieving the reflective polarization conversation and co-polarized transmission for the backward incident LP wave while preserving the EM energy harvesting and transmission for the forward incident wave. In addition, to explore the flexibility of the JMA in more general scenarios, double anti-direction AE SSPPs with different sizes are nested to acquire non-overlapped energy-harvesting bands for the opposite-direction incident waves. The emerging direction-selective JMS based on the anapole response can acquire copious EM functionalities, including energy harvesting, reflective polarization conversation, and co-polarized transmission under bidirectional incident waves, differing completely from previously reported anapole and Janus metamolecules. The series of anapole-excited multifunctional metastructures achieved by utilizing the directional characteristics of EM wave has extended the brand new field of multipole electrodynamics and facilitated the diverse high-responsive functional integration for compact integrated optical devices.

## 2. Design and discussion

### 2.1. Anapole-excited metastructure

The configuration and operating mechanism of such a metastructure based on the anapole mode are illustrated in Fig. 1(a). The elliptical gold configuration can be divided into two parts by the split rectangular gold patches, namely the upper and lower semioval metallic rings, which are printed on the inner wall of the square dielectric cavity with a relative permittivity of 4.45 + i0.089.[53] For the forward normally incident transverse electric (TE) wave with the electric and magnetic vectors
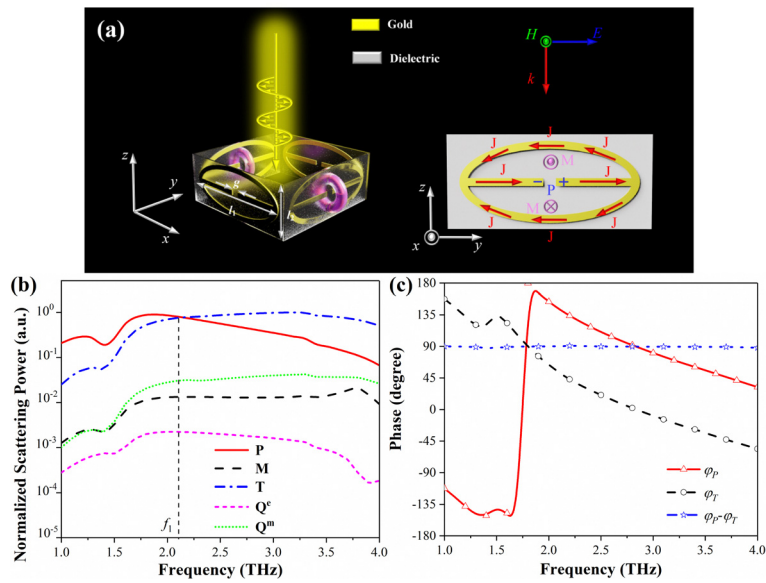
11376 | *Phys. Chem. Chem. Phys.*, 2023, **25**, 11375–11386

This journal is © the Owner Societies 2023

**Fig. 1** (a) Schematic for the configuration and operation mechanism of the AE metastructure cell for the TE wave: $J$ is the induced currents (red arrows), $P$ is the electric dipole moment (blue "+" and "−"), $M$ is the magnetic dipole moment (purple arrows), and the purple torus indicates the head-to-tail ring of the magnetic dipole $M$, thus inducing the toroidal dipole moment $T$, $l_1 = 57$ μm, $l_2 = 7$ μm, and $g = 2$ μm. (b) The dispersion of the normalized scattering power for five EM multipoles depending on the split elliptical-ring metamaterial (unit cell) for the TE wave. $P$: electric dipole, $M$: magnetic dipole, $T$: toroidal dipole, $Q^e$: electric quadrupole, $Q^m$: magnetic quadrupole, and $f_1 = 2.17$ THz. (c) The phase of the electric $P$ and magnetic $M$ dipole moments, and their phase difference for the TE wave.

pointing toward $+y$- and $+x$-directions, respectively, the electric field can stimulate the charge oscillation $\rho$ (see eqn (1)) across the gap in the elliptical-ring metallic resonators parallel to the electric field vector (the blue "+" and "−" in Fig. 1(a)), thus inducing a robust electric dipole $P$ (the red arrows in Fig. 1(a)) toward the $y$-direction (see eqn (2)). Subsequently, the oscillating charges can produce the reverse-rotating oscillating currents each flowing along the upper and lower semioval rings, yielding a pair of anti-parallel magnetic dipole moments $M$ (the purple arrows in Fig. 1(a)) and then inducing the toroidal dipole moment $T$ also oriented toward the $y$-direction and lagging $\pi/4$ behind the electric dipole moment $P$ (see eqn (3)).

$$\rho(t) = \rho_0 e^{i\omega t} \quad (1)$$

$$P(t) = Pe^{i\omega t} \propto + y\rho_0 e^{i\omega t} \quad (2)$$

$$T(t) = Te^{i\omega t} \propto - yi\omega\rho_0 e^{i\omega t} \quad (3)$$

The radiated EM fields, $E_p(t)$, $H_p(t)$, $E_T(t)$, and $H_T(t)$, each originating from the electric $P$ and toroidal $T$ dipole moments, can be calculated according to eqn (4)–(7), where $c$ is the speed of light in free space, $k$ is the wave number, and the functions of $D$, $F$, and $G$ can be found in Sections 1 and 2 of the ESI.†[34,54] Note that the toroidal dipole possesses the distinct feature of enabling radiation with the identical angular momentum to the electric dipole. Therefore, owing to the toroidal dipole's lagging $\pi/4$ behind the electric dipole, the phase difference of their radiated fields can always maintain $\pi/2$. In addition, the amplitudes of induced oscillating currents increase gradually with the wavelength of the incident wave close to the circumference of the split elliptical ring, resulting in the enhancement

of the toroidal dipole emission to cancel the radiation of the electric dipole moment, further inducing the anapole mode. Similarly, the transverse magnetic (TM) wave with electric and magnetic vectors pointing toward $-x$- and $+y$-directions can also induce the anapole mode existing in the gold split elliptical-ring structures parallel to the $x$-direction. According to the calculated normalized scattering power and phase of multipoles for the TE wave depicted in Fig. 1(b) and (c), the scattering powers of electric $P$ and toroidal $T$ dipole moments dominate over those of other multipoles in a wide frequency band and further becomes identical at $f_1 = 2.17$ THz. Meanwhile, the phase of $P$ leads by $\pi/4$ ahead of $T$, which further verifies the theoretical analysis mentioned above.

$$E_p(t) = \left[\frac{F(\omega, r)(r \times P)}{c^2 r^2} r - \frac{G(\omega, r)}{c^2} P\right]\frac{\exp(-ikr + i\omega t)}{r} \quad (4)$$

$$H_p(t) = -\frac{ikD(\omega, r)}{cr}[r \times P]\frac{\exp(-ikr + i\omega t)}{r} \quad (5)$$

$$E_T(t) = \left[\frac{ikG(\omega, r)}{c^2} T - \frac{ikF(\omega, r)(r \times T)}{c^2 r^2} r\right]\frac{\exp(-ikr + i\omega t)}{r} \quad (6)$$

$$H_p(t) = -\frac{k^2 D(\omega, r)}{cr}[r \times T]\frac{\exp(-ikr + i\omega t)}{r} \quad (7)$$

Considering the electric and toroidal dipoles placed at the origin ($r = 0$), the total electric and magnetic fields, $E_{total}(t)$ and $H_{total}(t)$, radiated by the superposition of such double dipoles

This journal is © the Owner Societies 2023

*Phys. Chem. Chem. Phys.*, 2023, **25**, 11375–11386 | **11377**

can be expressed by eqn (8) and (9).

$$\boldsymbol{E}_{\text{total}}(t) =$$
$$\left[ \frac{F(\omega, r)\boldsymbol{r} \times (\boldsymbol{P} - ik\boldsymbol{T})}{c^2 r^2} \boldsymbol{r} - \frac{G(\omega, r)}{c^2}(\boldsymbol{P} - ik\boldsymbol{T}) \right] \frac{\exp(-ikr + i\omega t)}{r}$$

(8)

$$\boldsymbol{H}_{\text{total}}(t) = -\frac{ikD(\omega, r)}{cr}[\boldsymbol{r} \times (\boldsymbol{P} - ik\boldsymbol{T})]\frac{\exp(-ikr + i\omega t)}{r} \quad (9)$$

Note that the radiated fields of the anapole mode in the case of $\boldsymbol{P} = ik\boldsymbol{T}$ will disappear in the far field ($r \neq 0$) due to the strong destructive interference originating from the electric and toroidal dipole moments. Meanwhile, their constructive interference can confine the EM energy to one point at $r = 0$, which can be illustrated by the $\delta$ function:

$$\boldsymbol{E}_{\text{total}(r=0)} = ik\boldsymbol{T}\delta(\boldsymbol{r})\exp(i\omega t) \quad (10)$$

$$\boldsymbol{H}_{\text{total}(r=0)} = ik\text{rot}[\boldsymbol{T}\delta(\boldsymbol{r})]\exp(i\omega t) \quad (11)$$

It can be seen in eqn (10) and (11) that the electric field is mainly localized in one point ($r = 0$) while the magnetic field can form a closed-loop configuration with normal parallel to the electric-field vector.

To verify the operating mechanism and EM characteristics of such an AEM, the EM simulation software High Frequency Structure Simulator (HFSS) is introduced, thus acquiring the distribution of induced currents and magnetic-field vectors in the vicinity of the AE metastructure depicted in Fig. 2(a) and (b). It can be observed that the counter-rotating currents $J$

induced by the TE and TM waves at $f_1$ can each flow along the gold elliptical-ring structures each parallel to $y–z$ and $x–z$ planes, consequently forming the head-to-tail loops of magnetic dipole moments $\boldsymbol{M}$ orthogonal to the $y$- and $x$-directions, respectively. Furthermore, the induced out-of-plane loops of magnetic dipoles $\boldsymbol{M}$ for the TE and TM waves can be equivalent to the toroidal dipole moments pointing towards the $y$- and $x$-directions, which satisfies the theoretical analysis mentioned above. Meanwhile, the localized magnetic field in the vicinity of the unit cell for the TE and TM waves can construct the head-to-tail configuration in $x–z$ and $y–z$ planes each orthogonal to the electric field vectors, which is the distinctive hallmark of anapole resonance according to eqn (11).[51,52] To sum up, the distribution of induced currents and magnetic-field vectors effectively verifies the fabrication mechanism of the anapole mode existing in such a square-cavity metastructure.

In the optical microcavities currently applied in controlling the light emission in quantum optics and telecommunication, the mode volume $V_m$ is regarded as the critical quantitative factor in describing the spatial confinement of energy density, which is anti-proportional to the effect of EM localization.[55,56] Owing to the constructive and destructive interference originating from anapole resonance in such a square microcavity with elliptical gold rings, most EM energy of the incident light at $f_1$ is confined to the circular area in the AEM, thus leading to the decrease of $V_m$ to $4.1 \times 10^{-5} (\lambda/n)^3$ (extraction details in Section 3 of the ESI†), signifying that the microcavity excited by the anapole mode can strongly couple to the incident wave to confine the EM energy. The near-field enhancement of EM energy based on the anapole response can further increase the
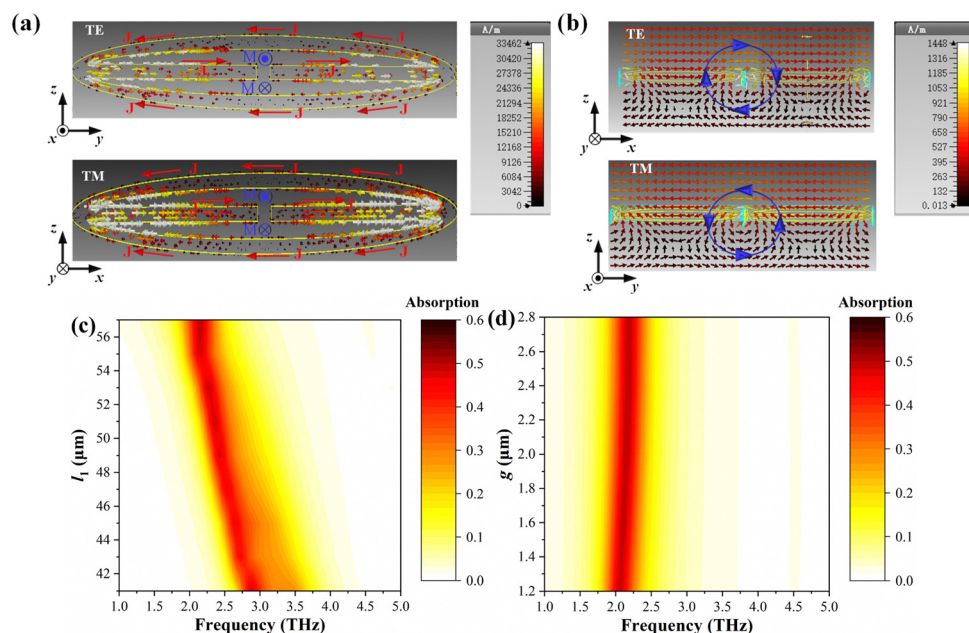


Fig. 2 EM responses of the AE metastructure for the normal-incident horizontal-polarized waves. (a) The distribution of induced current vectors in the unit cell for the TE and TM waves at the anapole-resonant frequency of $f_1$. (b) The distribution of magnetic field vectors in the vicinity of the metastructure for the TE and TM waves at the anapole-resonant frequency of $f_1$. (c) The effect of the major fast axis $l_1$ of the elliptical ring on the energy harvesting efficiency for the TE wave in the AE metamaterial. (d) The effect of the gap $g$ existing in the elliptical ring on the energy harvesting efficiency for the TE wave in the AE metamaterial.

11378 | *Phys. Chem. Chem. Phys.*, 2023, **25**, 11375–11386

This journal is © the Owner Societies 2023

decay rate, consequently causing the decrease of dephasing time, which can be calculated as 1.43 ps at $f_1$ (extraction details in Section 4 of the ESI†). Additionally, note that the EM power harvesting $P$ in the non-magnetic medium mainly depends on the dielectric and metallic losses, and the electric field strength, complying with the relationship of $P = 1/2(\omega\varepsilon'' + \sigma)|E|^2$, where $\omega$, $\varepsilon''$, $\sigma$, and $E$ indicate the angular frequency, the imaginary part of permittivity, the conductivity, and the electric-field strength, respectively.[57] Therefore, with the enhancement of electric-field energy density in the proposed configuration relying on the anapole resonance, the absorbed EM energy also increases

considerably. According to the theory of multiple reflection and interference, the EM energy absorption can be expressed as[58]

$$A(\omega) = 1 - R(\omega) - T(\omega) = 1 - |S_{11}|^2 - |S_{21}|^2 \quad (12)$$

where $A(\omega)$ is the absorption, $R(\omega)$ (i.e., $|S_{11}|^2$) is the super-position of co-polarized and cross-polarized reflection, and $T(\omega)$ (i.e., $|S_{21}|^2$) is the superposition of co-polarized and cross-polarized transmission. Fig. 2(c) and (d) illustrate the EM absorption of TE waves in the AEM with split elliptical rings of different sizes and gaps. It can be seen in Fig. 2(c) that the
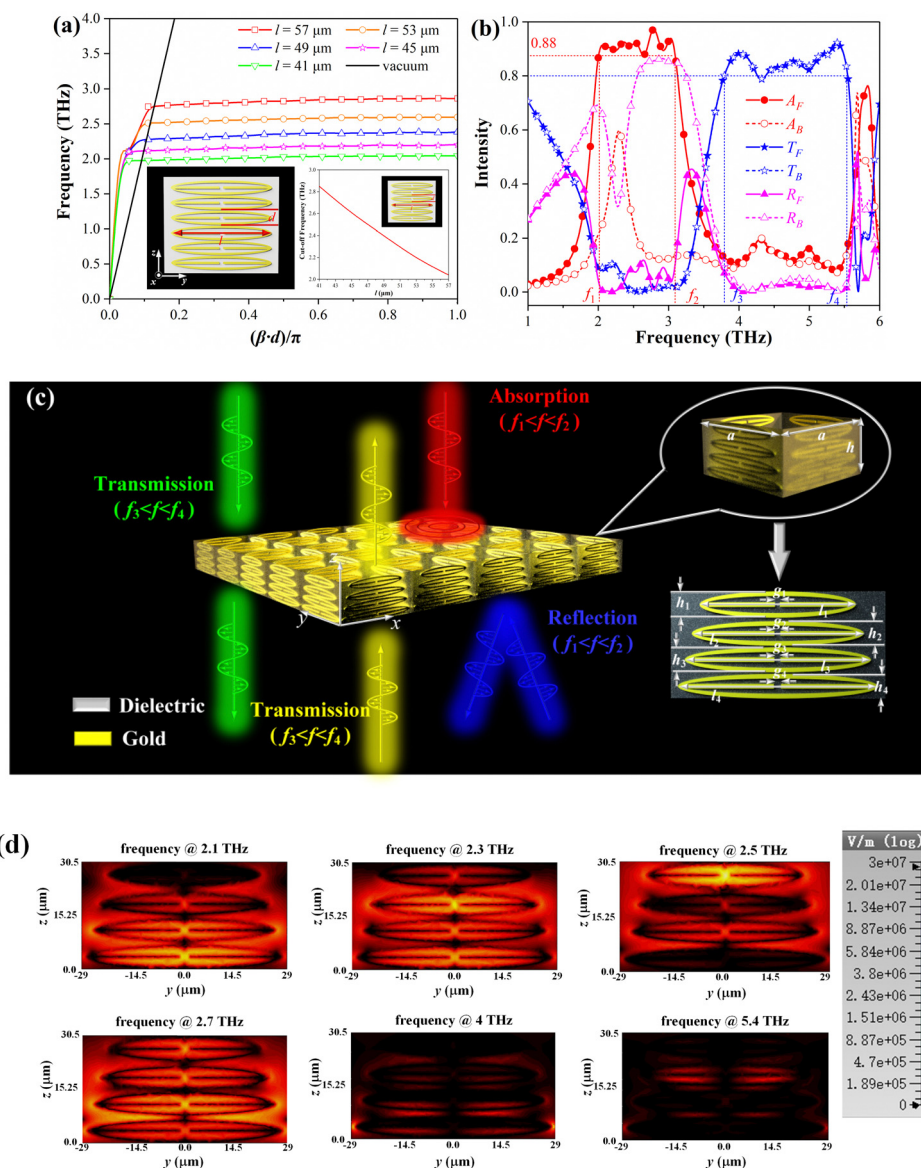


Fig. 3  (a) The dispersion curve of AE SSPP with metallic elliptical rings of different sizes. (b) The EM characteristics of the unidirectional MSR based on the gradient AE SSPP for the TE wave: $A_F$ and $A_B$ are the absorption for the forward and backward incident waves, $T_F$ and $T_B$ are the co-polarized transmission for the forward and backward incident waves, $R_F$ and $R_B$ are the co-polarized reflection for the forward and backward incident waves, $f_1$ = 2 THz, $f_2$ = 3.08 THz, $f_3$ = 3.77 THz, and $f_4$ = 5.55 THz. (c) Schematic for the configuration and function of the unidirectional MSR based on the gradient AE SSPP: $l_1$ = 44.5 μm, $l_2$ = 49 μm, $l_3$ = 53 μm, $l_4$ = 57 μm, $h_1$ = 7.5 μm, $h_2$ = 7 μm, $h_3$ = 7 μm, $h_4$ = 7 μm, $g_1$ = 1.4 μm, $g_2$ = 1.7 μm, $g_3$ = 1.7 μm, and $g_4$ = 2 μm. (d) The distribution of the electric field strength $|E|$ in the unidirectional MSR based on the gradient AE SSPP for the forward incident TE wave at different frequencies.

This journal is © the Owner Societies 2023

Phys. Chem. Chem. Phys., 2023, 25, 11375–11386 | 11379

absorption peak gradually shifts to a lower frequency as the fast-axial length $l_1$ of the elliptical rings increases because the resonant wavelength of the incident wave has to increase to approach the raised circumference of elliptical rings, thus enhancing the toroidal dipole power to cancel the electric dipole scattering completely, namely inducing the anapole mode in the lower frequency which can strongly confine the incident light with the larger wavelength to the configuration to acquire the high efficiency of EM energy harvesting. In contrast, the absorption peak moves to a higher frequency with the increase of gaps $g$ in the elliptical rings shown in Fig. 2(d), which is mainly because of the shift of the electric-dipole resonance to a higher frequency band. Therefore, the cross point of the electric- and toroidal-dipole moments will move to the higher frequency, thus inducing the higher-frequency anapole mode to harvest the incident wave with high efficiency.

## 2.2. Directional multifunctional JMS based on AE SSPP

The AE SSPP is performed based on a row of periodic metallic elliptical rings printed on the dielectric layer with a thickness of 0.5 μm ($\varepsilon_r = 4.454.45 + i0.089^{53}$) along the $z$-direction, where there is always a gap of 1 μm between the adjacent elliptical rings. The geometric sizes of the metallic structure have an essential influence on the dispersion relationship of the SSPP mode according to a previous research,[59,60,65] thus investigating the relationship between the dispersion curve and fast-axial length $l$ for the TE wave as illustrated in Fig. 3(a). Within the first Brillouin zone, the dispersion curves are above the light line (black line), a hallmark of the fast-wave and radiated mode, and further gradually get away from and below the light line, finally reaching the cut-off frequency of the SSPP mode, which can be contributed to the excellent field-confinement ability of the anapole mode depending on the elliptical-ring configuration. Additionally, it is worth noting that with the increase of the fast-axial length $l$ of the unit elliptical ring, the cut-off frequency gradually shifts to the lower frequency, which is mainly because the resonant frequency of the anapole mode decreases corresponding to the improvement of the size of the elliptical ring presented in Fig. 2(c).

By utilizing the dispersion characteristic of AE SSPP, the unidirectional MSR consisting of gradient metallic elliptical rings is fabricated, as illustrated in Fig. 3(c). The gradient metallic elliptical-ring structures with reduced sizes are arranged successively on the inner wall of a square dielectric cavity with a thickness of 0.5 μm along the +$z$-direction in the unit cell of such an AEM, where the gaps between the adjacent metallic rings always maintain 1 μm (the detailed sizes are depicted in Fig. 3(c)). Compared with the SSPP based on the uniform metallic elliptical rings, the designed metastrucure composed of the gradient metallic configuration exhibits the brilliant direction-selective properties by fully taking advantage of the excellent field-localization capacity for the incident waves at different frequencies corresponding to the elliptical rings of different sizes. Supposing that the cut-off frequencies of the largest and smallest elliptical rings in the unidirectional AE MSR are set as $f_1$ and $f_2$, as the forward vertical-incident wave is located at the region between

$f_1$ and $f_2$ (*i.e.*, $f_1 \leqq f \leqq f_2$), the abundant EM energy of incident light is confined to the vicinity of the corresponding elliptical-ring configuration owing to the effect of the anapole response, thus enhancing the EM intensity in the proposed metadevice and further acquiring the high absorption of EM energy relying on the dielectric and metallic losses. However, the backward vertical-incident light working at the regime of $f_1 < f \leqq f_2$ can be reflected by the largest elliptical-ring structure in the bottom except for the incident wave at $f_1$ can be confined around the bottom metallic ring supported by the corresponding anapole resonance. Furthermore, as the wavelength of the bidirectional vertical-incident waves continues to be shortened but still longer than the period of the elliptical-ring structure (*i.e.*, $f_2 < f < f_3$), most of the incident light cannot be confined by the gradient elliptical rings and will be reflected. However, the forward and backward vertical-incident waves with a shorter wavelength than the period (*i.e.*, $f_3 < f < f_4$) can be transmitted through the gap existing between the metallic elliptical rings.

To validate the effects of the incident direction of waves on the unidirectional AE MSR mentioned above, we investigate the EM responses of the proposed metastrucure under the bidirectional TE wave incidence, as illustrated in Fig. 3(b). Owing to the direction-selective characteristic of such a metastrucure based on the AE SSPP, the unidirectional MSR can acquire an absorption over 0.88 in a band of 2–3.08 THz (42.5%), and simultaneously a peak co-polarized transmission of 0.92 at 5.39 THz with a transmission (over 0.8) window covering 3.77–5.55 THz (38.2%) for the forward incident TE wave. Meanwhile, as the backward wave normally illuminates, the MSR also can attain the co-polarized window of 3.77–5.55 THz (38.2%) precisely identical to the forward vertical-incident wave, and can effectively reflect the backward incident wave without polarization conversation at 2.56–3.25 THz (23.75%), where the reflection is up to 0.8. Moreover, the backward vertical-incident wave at 2.29 THz can be harvested by the metastructure with an absorption of 0.61 based on the strong field-localization properties of the anapole mode existing in the bottom largest metallic elliptical-ring structure. It is worth noting that the simulated EM responses of the proposed metastructure for the bidirectional vertical-incident waves are nearly in accordance with the theoretical analysis above.

To further research the near-field localization characteristic of anapole modes existing in the gradient SSPP on the functionality of the MSR, the distribution of the electric-field strength $|E|$ under normal incidence has been acquired by simulations. Owing to the polarization-independence characteristic of MSR (extraction of details in Section 5 of ESI†), we just focus on the situation of the normal-incident TE wave at different frequencies presented in Fig. 3(d). It can be observed that as the waves operate at 2.1 THz, 2.3 THz, and 2.5 THz, the electric fields are mainly confined around the corresponding metallic elliptical-ring structures whose cut-off frequencies are in close relationship with the operating frequencies of incident waves shown in Fig. 3(a), *i.e.*, the fourth, second and first elliptical rings from the top to bottom, signifying that the anapole resonances relying on the corresponding metallic rings

11380 | *Phys. Chem. Chem. Phys.*, 2023, **25**, 11375–11386

This journal is © the Owner Societies 2023

can greatly confine the incident light to enhance the EM energy density in the metastructure, thus acquiring the high energy harvesting efficiency. In addition, the incident wave at 2.7 THz is mainly confined around but not inner to the metallic ring structures due to the strong coupling between the different metallic resonators. Simultaneously, as the working frequencies of the vertical-incident wave increase to 4 THz and 5.4 THz in the transmission window, there is nearly no electric field strength confined to the unit cell which means that the wave can go through the metastructure with high efficiency. To summarize, the distribution of the electric-field strength effectively demonstrates the aforementioned theoretical analysis of the functional mechanism of the unidirectional AE MSR.

The aforementioned unidirectional MSR based on the AE SSPP can manipulate the forward vertical-incident wave, i.e., EM energy harvesting and transmission in a wide band simultaneously, but also can reflect and transmit the backward normal-incident wave operating in a broad band without changing the polarization state. To combine the polarization control with the energy harvesting and transmission of the incident wave, the MSR is integrated with the PCS, the asymmetric H-shaped metallic structure, which can change the polarization state of the reflective backward incident wave and meanwhile attenuate the field-localization effect of the anapole mode existing in the bottom elliptical ring for the backward-incident wave, thus achieving the absorption and co-polarized transmission of the forward incident wave, and the reflective polarization conversation and co-polarized transmission of the backward incident wave, as presented in Fig. 4(a).

To clarify the operating mechanism of the PCS, the reflective polarization-conversation metadevice (PCM), mainly consisting of the asymmetric H-shaped structure, is shown in Fig. 4(b). The asymmetric H-shaped metallic configuration is printed on the dielectric layer ($\varepsilon_r = 4.454.45 + \mathrm{i}0.089^{53}$) with a thickness of 0.5 μm, which is arranged along the diagonal $y = x$ and perpendicular to the metallic background. For the forward incident TE wave, the electric field vector $E_{iy}$ can be decomposed into double mutual-vertical components $E_{iv}$ and $E_{iu}$ each along the diagonal ($y = x$) and its vertical direction ($y = -x$), where $E_{iv}$ can induce the oscillating currents in the H-shaped metallic structure along the diagonal, further inspiring the electric dipole $P$ pointing to the diagonal as shown in Fig. 4(c). Furthermore, the induced electric field of $P$ can also be decomposed into double components, $E_{rx}$ and $E_{ry}$, where one electric field component $E_{rx}$ is vertical to $E_{iy}$, resulting in the polarization conversation. It can be observed in Fig. 5(a) that as the TE wave operating at 2.1–2.9 THz (32%) is normally incident, the co-polarized reflection ($R_{yy} = |E_{ry}|^2/|E_{iy}|^2$) is remarkably restrained, and the cross-polarized reflection ($R_{xy} = |E_{rx}|^2/|E_{iy}|^2$) is increased to above 0.9, consequently acquiring the PCR of 0.9 (PCR = $R_{xy}/(R_{xy} + R_{yy})$).[61] Meanwhile, the length $l_1$ of the polarization-conversation structure along the diagonal can significantly affect the PCR (over 0.9) bandwidth, as depicted in Fig. 5(b), where the PCR bandwidth shifts to the lower frequency with the increase of $l_1$.

Since the AE MSR described previously is capable of reflecting most of the backward normal-incident wave in the range of 2.5–3.6 THz (reflection of 0.8 or more, as shown in Fig. 3(b)), the MSR structure can substitute the metallic background in the PCM to fabricate the multifunctional JMS, allowing the integration of copious functionalities containing the EM energy harvesting, transmission, and polarization control for different-direction incident waves, as depicted in Fig. 4(a). It is obvious that the distance $h$ between the AE MSR and PCS is a crucial parameter that controls the effect of the field-localization properties of the anapole mode supported by the bottom elliptical ring on the reflection and absorption of waves (extraction details in Section 6 of the ESI†). By optimizing the coupling between the AE MSR and PCS, the bidirectional normal-incident waves at 3.95–5.2 THz (27.3%) can effectively transmit through the multifunctional metastructure (the transmission of over 0.8) by taking advantage of the superior transmitted characteristic of SSPP depicted in Fig. 5(c) and (d). Meanwhile, the forward vertical-incident wave at 2.14–3.09 THz (36.3%) can induce the anapole modes existing in the elliptical rings of different sizes, thus greatly localizing the
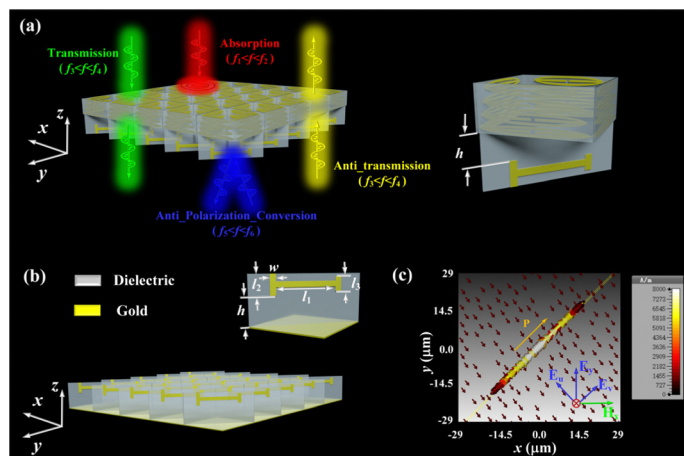


Fig. 4 (a) Schematic for the configuration and functionalities of the directional AE multifunctional JMS combined with the polarization-conversation structure. (b) Schematic for the reflective PCM and its unit cell: $l_1 = 36$ μm, $l_2 = 14$ μm, $l_3 = 10$ μm, $w = 4.2$ μm, and $h = 25$ μm. (c) The distribution of the induced current vector in the unit cell of the reflective PCM for the TE wave at 2.2 THz.

This journal is © the Owner Societies 2023

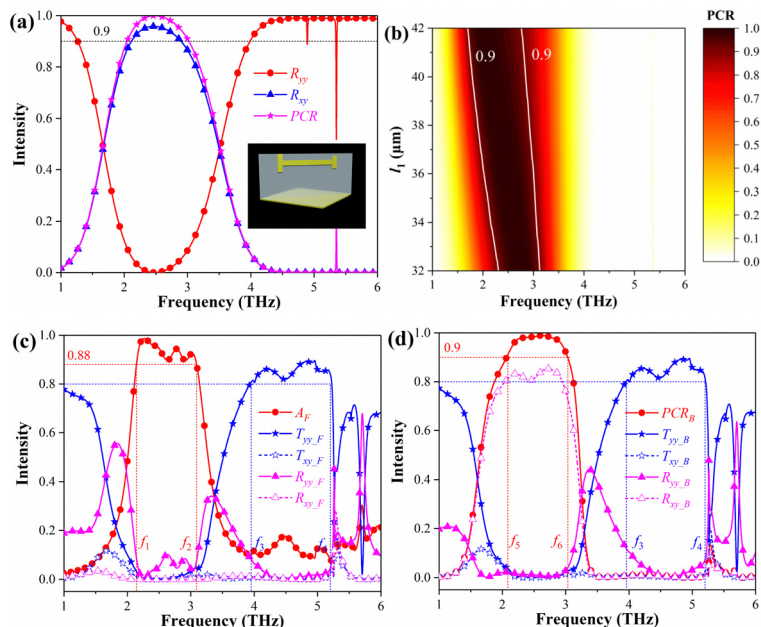*Phys. Chem. Chem. Phys.*, 2023, **25**, 11375–11386 | 11381

**Fig. 5** (a) The reflective characteristic (*i.e.*, the co-polarized reflection $R_{xx}$ and cross-polarized reflection $R_{xy}$) and polarization conversation rate (PCR) of the reflective PCM for the TE wave. (b) The variation of the PCR *versus* the size $l_1$ of the reflective PCM. (c) and (d) EM responses of the directional AE multifunctional JMS for the bidirectional TE waves: (c) the EM response corresponding to the forward incident wave: $A_F$ is the absorption, $T_{yy\_F}$ and $T_{xy\_F}$ are the co-polarized and cross-polarized transmission, and $R_{yy\_F}$ and $R_{xy\_F}$ are the co-polarized and cross-polarized reflection, $f_1$ = 2.14 THz, $f_2$ = 3.09 THz, $f_3$ = 3.95 THz, $f_4$ = 5.2 THz. (d) the EM response corresponding to the backward incident wave: PCR$_B$ is the polarization conversation rate, $T_{yy\_B}$ and $T_{xy\_B}$ are the co-polarized and cross-polarized transmission, and $R_{yy\_B}$ and $R_{xy\_B}$ are the co-polarized and cross-polarized reflection, $f_5$ = 2.08 THz, $f_6$ = 3.03 THz.

EM field to the cavity configuration to enhance the energy density and further achieving the high absorption over 0.88. In addition, most of the backward normal-incident TE waves at 2.08–3.03 THz (37.2%) can be effectively reflected and meanwhile transform the polarization state depending on the asymmetric H-shaped structure with a PCR of over 0.9, consequently attaining the cross-polarized reflection of over 0.8.

### 2.3. Directional JMA based on AE SSPP

Compared with the reported metastructure absorber just aimed at the single-directional incident wave,[58,62] the proposed directional JMA can effectively harvest the dual-directional incident EM waves operating at non-overlapped frequency bands by utilizing the substantial field-localization properties of the AE SSPP, thus achieving the flexible tunability of absorption and further extending the application field, as illustrated in Fig. 6(a). The JMA is fabricated depending on the nested structure, where metallic elliptical rings with increasing sizes are in turn printed on the inner side of the outer square dielectric cavity with a thickness of 0.9 μm along the −*z*-direction. In contrast, the elliptical ring size located on the inner dielectric square cavity with a thickness of 0.6 μm gradually decreases along the −*z*-direction. Owing to the size difference of the metallic elliptical-ring configuration on the inner and outer cavities, the corresponding cut-off frequencies are different as the EM waves are incident in the forward and reverse directions, further leading to the difference in the absorption bands. Meanwhile, to reduce the influence of the coupling between the inner and outer cavities on the absorption efficiency of the bidirectional incident waves,

the inner cavity structure of the JMA is shifted downward along the *z*-direction by a distance of $h_z$, whose obvious effect on the bidirectional absorption is illustrated in Section 7 of the ESI.†

Considering that the cut-off frequencies for the largest and smallest elliptical rings printed on the outer cavity are $f_1$ and $f_2$, and those on the inner structure correspond to $f_3$ and $f_4$, as the forward normal-incident horizontal-polarized wave operates in the band between $f_1$ and $f_2$ ($f_1 < f < f_2$), the anapole modes can be induced in the outer metallic elliptical-ring structure, thus greatly localizing the incident wave to further enhance the EM energy density in the vicinity of the proposed metadevice and acquire the high energy absorption. However, as the frequency of the incident wave continues to increase above $f_3$, due to the coupling between the outer and inner cavities, a part of the incident waves transmitting through the gaps between the outer adjacent metallic structures can be harvested, simultaneously some are reflected by the upper elliptical-ring configuration located at the inner square cavity. On the other hand, the backward normal-incident wave in the region between $f_3$ and $f_4$ ($f_3 < f < f_4$) also can induce the anapole modes existing in the inner elliptical-ring configuration, which can immensely improve the energy density in the proposed cavity, consequently harvested owing to the metallic and dielectric losses. Nevertheless, as the operating frequency of the backward incident wave decreases to the regime between $f_1$ and $f_2$ ($f_1 < f < f_2$), most of the incident wave can be reflected by the bottom elliptical ring according to the characteristic of the AE SSPP mentioned above. However, the backward incident wave at $f_1$ can excite the anapole resonance depending on the bottom
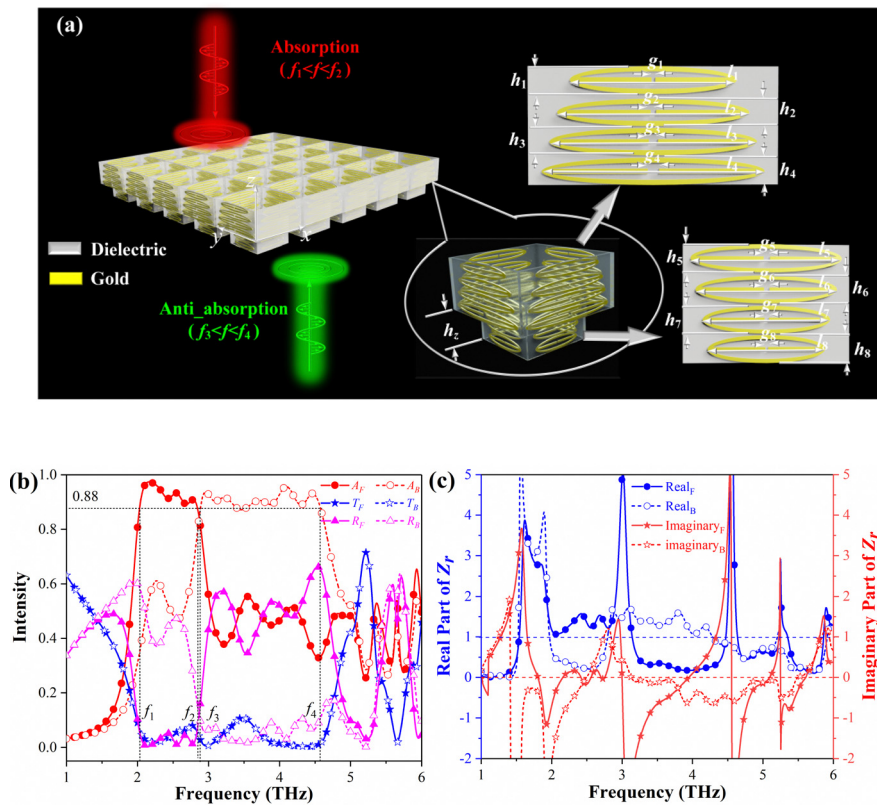
**11382** | *Phys. Chem. Chem. Phys.*, 2023, **25**, 11375–11386

This journal is © the Owner Societies 2023

**Fig. 6** (a) Schematic for the configuration and functionality of the directional JMA based on AE SSPP. The outer square cavity: $l_1 = 57$ μm, $l_2 = 53$ μm, $l_3 = 49$ μm, $l_4 = 42.5$ μm, $h_1 = 5.2$ μm, $h_2 = 6$ μm, $h_3 = 6$ μm, $h_4 = 6$ μm, $g_1 = 2.9$ μm, $g_2 = 2.3$ μm, $g_3 = 1.4$ μm, and $g_4 = 1$ μm. The inner square cavity: $l_5 = 38$ μm, $l_6 = 35.5$ μm, $l_7 = 32$ μm, $l_8 = 29.5$ μm, $h_5 = 6$ μm, $h_6 = 6$ μm, $h_7 = 6$ μm, $h_8 = 6$ μm, $g_5 = 0.7$ μm, $g_6 = 1.1$ μm, $g_7 = 1.4$ μm, $g_8 = 1.6$ μm, and $h_z = 16$ μm. (b) EM responses of the JMA for the forward and backward incident TE waves: $A_F$ and $A_B$ are the absorption for the forward and backward waves, $T_F$ and $T_B$ are the co-polarized transmission for the forward and backward waves, and $R_F$ and $R_B$ are the co-polarized reflection for the forward and backward waves. (c) The normalized equivalent complex intrinsic impedance $Z_r$ of the proposed JMA for the forward and backward incident TE waves: the real (blue lines) and imaginary (red lines) parts of $Z_r$.

elliptical ring, which can further confine most of the EM energy and attain high absorption. To verify the analysis of the operating mechanism of the directional JMA, the EM responses of the proposed JMA for the bidirectional incident TE waves are simulated, as illustrated in Fig. 6(b). It can be noted that the JMA can effectively harvest the forward vertical-incident EM wave at 2.02–2.84 THz (33.7%) with an absorption over 0.88, and can attain the absorption band of 2.88–4.58 THz (45.6%) for the backward normal-incident wave. Simultaneously, the EM characteristics in other bands under the bidirectional incident TE waves are also consistent with the formal theoretical analysis. There are similar non-overlapped absorption bands for bidirectional incident TM waves due to the polarization insensitivity of the JMA (extraction details in Section 7 of the ESI†).

Moreover, according to the impedance matching theory, the EM energy harvesting of the JMA for the vertical-incident wave can be quantitatively characterized by the normalized equivalent surface impedance expressed by eqn (13) and (14)

$$A(\omega) = 1 - R(\omega) - T(\omega) = 1 - \left| \frac{Z_r - 1}{Z_r + 1} \right|^2 \qquad (13)$$

$$Z_r = \sqrt{\frac{(1 + S_{11}(\omega))^2 - S_{21}(\omega)^2}{(1 - S_{11}(\omega))^2 - S_{21}(\omega)^2}} \qquad (14)$$

where $A(\omega)$ is the absorption, $R(\omega)$ is the superposition of the co- and cross-polarized reflection, $T(\omega)$ is the superposition of the co- and cross-polarized transmission, $Z_r = Z/Z_0$ is the normalized complex equivalent surface impedance ($Z$ is the equivalent surface impedance of the proposed metastructure, and $Z_0$ is the impedance in free space), $S_{11}(\omega)$ and $S_{21}(\omega)$ are the scattering parameters of reflection and transmission.[63,64] Note in eqn (13) and (14) that the absorption can approach the maximum as the normalized equivalent surface impedance is equal to 1, implying that the impedance of such an absorber can match well with the free space. In the light of the simulated complex equivalent surface impedance of the JMA under the forward and backward normal-incident waves as presented in Fig. 6(c), the real and imaginary parts of the normalized equivalent surface impedance are close to 1 and 0, respectively, in the absorption bands of the JMA for the bidirectional EM waves, *i.e.*, 2.02–2.84 THz (33.7%) and 2.88–4.58 THz (45.6%), which indicates that the JMA can well match the free space, thus realizing the localization of EM energy and greatly improving the absorption efficiency.

This journal is © the Owner Societies 2023

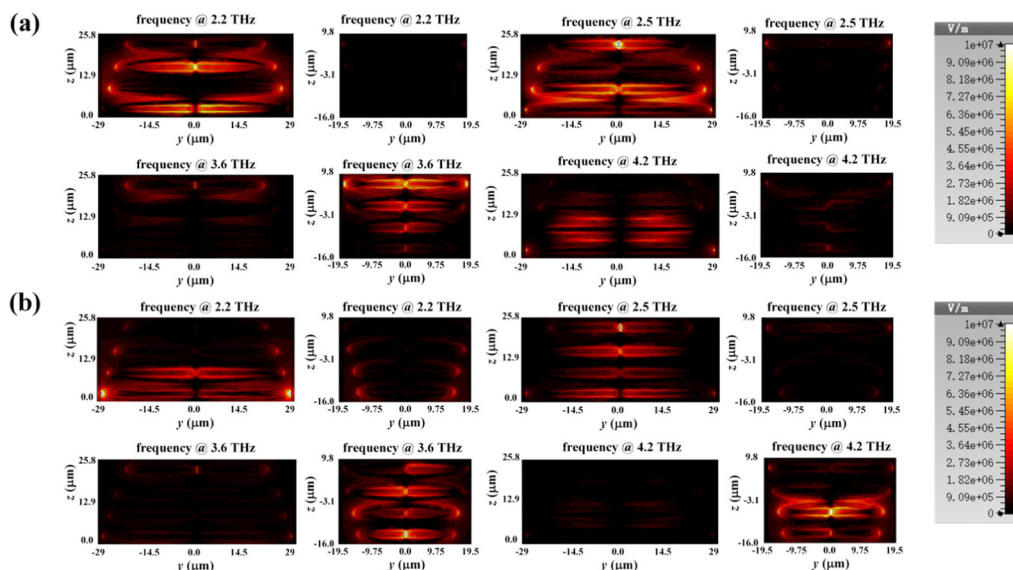*Phys. Chem. Chem. Phys.*, 2023, **25**, 11375–11386 | **11383**

Fig. 7 The distribution of the electric field in the outer (left) and inner (right) square cavity of the proposed directional JMA for the forward and backward vertical-incident TE waves at different frequencies: (a) the forward incident wave and (b) the backward incident wave.

The electric field distribution of the JMA for the bi-directional normal-incident waves also can effectively confirm the theoretical analysis of the absorption mechanism, as depicted in Fig. 7. For the forward vertical-incident waves at 2.2 THz and 2.5 THz, their electric fields are mainly concentrated around the outer metallic elliptical-ring structure, which is due to the strong localizing effect of the induced anapole resonance, while there is no distribution of the electric field in the inner cavity. As the frequency continues to increase to 3.6 THz, the electric field is mainly localized around the inner top elliptical-ring structures due to the corresponding anapole resonance, and only a tiny amount of the electric field is distributed in the outer layer. However, the forward incident wave at 4.2 THz is mainly distributed between the outer metallic rings, indicating that the wave propagating along the gap is localized because of the coupling effect between the inner and outer layers. For the backward vertical-incident EM wave, the electric field at 2.2 THz is mainly confined around the outer bottom elliptical-ring configuration depending on the localizing properties of the corresponding anapole resonance. Similarly, a part of the backward incident wave at 2.5 THz is located around the metallic structures in the outer cavity. However, as the operating frequency of the backward normal-incident wave continues to increase to 3.6 THz and 4.2 THz, the waves can induce the anapole resonances in the corresponding inner metallic structure, consequently confined around the metallic configuration. The simulated electric field distribution of the JMA for the TE waves in forward and reverse directions again proves the previous analysis of the working mechanism of the JMA.

## 3. Conclusions

Multiple directional Janus multifunctional THz metadevices based on the directional-selective AE SSPP are proposed in this paper. By utilizing the nonradiative EM characteristics of the anapole mode and directional-transmitted capacity sustained by the SSPP, which are verified by the dispersion of multipole scattering power and phase, and the distribution of the magnetic field and current vectors, an MSR for the forward vertical-incident wave is designed to acquire a polarization-insensitive absorption band of 2–3.08 THz (42.5%) and a co-polarized transmission window of 3.77–5.55 THz (38.2%). Furthermore, the multifunctional JMS, the combination of the MSR and PCS, is tailored to achieve an absorption band of 2.14–3.09 THz (36.3%) for the forward normal-incident wave, and a cross-polarized reflection band of 2.08–3.03 THz (37.2%) for the backward vertical-incident wave while attaining an identical co-polarized transmission window of 3.95–5.2 THz (27.3%). Meanwhile, to boost the flexible tunability of the absorption band, a JMA consisting of the reverse-directional AE SSPP is fabricated, thus attaining polarization-insensitive non-overlapped absorption bands of 2.02–2.84 THz (33.7%) and 2.88–4.58 THz (45.6%) for the bidirectional normal-incident waves. The series of Janus metadevices based on anapole resonance proposed in this paper takes full advantage of the selective properties of the AE SSPP on the direction of EM wave incidence to effectively integrate a variety of functional devices with excellent potential application prospects, furthermore opening up the pristine application field of multipole electrodynamics, especially for the selective wave front regulation.

## Conflicts of interest

There are no conflicts to declare.

## Acknowledgements

11384 | Phys. Chem. Chem. Phys., 2023, 25, 11375–11386

This journal is © the Owner Societies 2023

## Notes and references

1 N. Liu, H. Guo, L. Fu, S. Kaiser, H. Schweizer and H. Giessen, *Nat. Mater.*, 2007, **7**, 31–37.

2 A. Boltasseva and H. A. Atwater, *Science*, 2011, **331**, 290–291.

3 N. I. Zheludev and Y. S. Kivshar, *Nat. Mater.*, 2012, **11**, 917–924.

4 T. Xu and H. J. Lezec, *Nat. Commun.*, 2014, **5**, 4141.

5 Y. H. Wang, R. C. Jin, J. Li, J. Q. Li and Z. G. Dong, *Opt. Express*, 2018, **26**, 3508–3517.

6 I. V. Iorsh, I. S. Mukhin, I. V. Shadrivov, P. A. Belov and Y. S. Kivshar, *Phys. Rev. B: Condens. Matter Mater. Phys.*, 2013, **87**, 075416.

7 S. Basak, O. Bar-On and J. Scheuer, *Adv. Opt. Mater.*, 2020, **9**, 2001305.

8 Q. Xu, X. Su, C. Ouyang, N. Xu, W. Cao, Y. Zhang, Q. Li, C. Hu, J. Z. Gu, Z. Tian and A. K. Azad, *Opt. Lett.*, 2016, **41**, 4562–4565.

9 Y. Fan, T. Qiao, F. Zhang, Q. Fu, J. Dong, B. Kong and H. Li, *Sci. Rep.*, 2017, **7**, 40441.

10 A. Cerjan and S. Fan, *Phys. Rev. Lett.*, 2017, **118**, 253902.

11 R. Bekenstein, Y. Kabessa, Y. Sharabi, O. Tal, N. Engheta, G. Eisenstein, A. J. Agranat and M. Segev, *Nat. Photonics*, 2017, **11**, 664–670.

12 N. Landy and D. R. Smith, *Nat. Mater.*, 2012, **12**, 25–28.

13 M. K. Lee and Y. Y. Kim, *Sci. Rep.*, 2016, **6**, 20731.

14 P. N. Dyachenko, S. Molesky, A. Y. Petrov, M. Störmer, T. Krekeler, S. Lang, M. Ritter, Z. Jacob and M. Eich, *Nat. Commun.*, 2016, **7**, 11809.

15 A. R. Davoyan and N. Engheta, *ACS Photonics*, 2019, **6**, 581–586.

16 Q. He, S. Sun, S. Xiao and L. Zhou, *Adv. Opt. Mater.*, 2018, **6**, 1800415.

17 J. Jang, H. Jeong, G. Hu, C. Qiu, K. T. Nam and J. Rho, *Adv. Opt. Mater.*, 2019, **7**, 1801070.

18 J. H. Kang, S. J. Lee, B. J. Kang, W. T. Kim, F. Rotermund and Q. H. Park, *ACS Appl. Mater. Interfaces*, 2018, **10**, 19331–19335.

19 R. C. Devlin, A. Ambrosio, N. A. Rubin, J. P. B. Mueller and F. Capasso, *Science*, 2017, **358**, 896–901.

20 G. Li, G. Sartorello, S. Chen, L. H. Nicholls, K. F. Li, T. Zentgraf, S. Zhang and A. V. Zayats, *Laser Photonics Rev.*, 2018, **12**, 1800034.

21 P. G. de Gennes, *Science*, 1992, **256**, 495–497.

22 G. Shang, H. Li, Z. C. Wang, S. N. Burokur, K. Zhang, J. Liu, Q. Wu, X. M. Ding and X. M. Ding, *ACS Appl. Electron. Mater.*, 2021, **3**, 2638–2645.

23 K. Chen, G. W. Ding, G. W. Hu, Z. W. Jin, J. M. Zhao, Y. J. Feng, T. Jiang, A. Alù and C. W. Qiu, *Adv. Mater.*, 2019, **32**(2), 1906352.

24 H. X. Xu, C. H. Wang, G. W. Hu, Y. Z. Wang, S. W. Tang, Y. J. Huang, X. W. Lin, W. Huang and C. W. Qiu, *Adv. Opt. Mater.*, 2021, **9**, 2100190.

25 Y. Chen, X. D. Yang and J. Gao, *Light: Sci. Appl.*, 2019, **8**, 1028.

26 G. Y. Shang, G. W. Hu, C. S. Guan, Y. Wang, K. Zhang, Q. Wu, J. Liu, X. M. Ding, S. N. Burokur, H. Y. Li and C. W. Qiu, *Nanophotonics*, 2022, **11**, 3729.

27 D. L. Sounas and C. Caloz, *Appl. Phys. Lett.*, 2011, **98**, 021911.

28 Z. Wang, Y. Chong, J. D. Joannopoulos and M. Soljačić, *Nature*, 2009, **461**, 772–775.

29 A. M. Mahmoud, A. R. Davoyan and N. Engheta, *Nat. Commun.*, 2015, **6**, 8359.

30 L. Zhang, X. Q. Chen, R. W. Shao, J. Y. Dai, Q. Cheng, G. Castaldi, V. Galdi and T. J. Cui, *Adv. Mater.*, 2019, **31**, 1904069.

31 D. L. Sounas and A. Alù, *Nat. Photonics*, 2017, **11**, 774–783.

32 K. Marinov, A. D. Boardman, V. A. Fedotov and N. Zheludev, *New J. Phys.*, 2007, **9**, 324.

33 I. B. Zel'Dovich, *J. Exp. Theor. Phys.*, 1958, **6**, 1184–1186.

34 G. N. Afanasiev and Y. P. Stepanovsky, *J. Phys. A: Math. Gen.*, 1995, **28**, 4565–4580.

35 V. Savinov, V. A. Fedotov and N. I. Zheludev, *Phys. Rev. B: Condens. Matter Mater. Phys.*, 2014, **89**, 205112.

36 T. Kaelberer, V. A. Fedotov, N. Papasimakis, D. P. Tsai and N. I. Zheludev, *Science*, 2010, **330**, 1510–1512.

37 M. Gupta, Y. K. Srivastava and R. Singh, *Adv. Mater.*, 2017, **30**, 1704845.

38 Z. Liu, S. Du, A. Cui, Z. C. Li, Y. C. Fan, S. Q. Chen, W. X. Li, J. J. Li and C. Z. Gu, *Adv. Mater.*, 2017, **29**, 1606298.

39 A. Ahmadivand, B. Gerislioglu, R. Ahuja and Y. K. Mishra, *Laser Photonics Rev.*, 2020, **14**, 1900326.

40 A. Ahmadivand, B. Gerislioglu, R. Ahuja and Y. K. Mishra, *Mater. Today*, 2020, **32**, 108–130.

41 M. Gupta and R. Singh, *Rev. Phys.*, 2020, **5**, 100040.

42 A. E. Miroshnichenko, A. B. Evlyukhin, Y. F. Yu, R. M. Bakker, A. Chipouline, A. I. Kuznetsov, B. Luk'yanchuk, B. N. Chichkov and Y. S. Kivshar, *Nat. Commun.*, 2015, **6**, 9069.

43 T. Y. Zhang, Y. Che, K. Chen, J. Xu and X. Li, *Nat. Commun.*, 2020, **11**, 15476.

44 V. A. Fedotov, A. V. Rogacheva, V. Savinov, D. P. Tsai and N. I. Zheludev, *Sci. Rep.*, 2013, **3**, 02967.

45 G. Grinblat, Y. Li, M. P. Nielsen, R. F. Oulton and S. A. Maier, *ACS Nano*, 2016, **11**, 953–960.

46 J. S. T. Gongora, A. E. Miroshnichenko, Y. S. Kivshar and A. Fratalocchi, *Nat. Commun.*, 2017, **8**, 15535.

47 L. Wei, Z. Xi, N. Bhattacharya and H. P. Urbach, *Optica*, 2016, **3**, 799–802.

48 A. K. Ospanova, G. Labate, L. Matekovits and A. A. Basharin, *Sci. Rep.*, 2018, **8**, 12514.

49 A. Ahmadivand, B. Gerislioglu, P. Manickam, A. Kaushik, S. Bhansali, M. Nair and N. Pala, *ACS Sens.*, 2017, **2**, 1359–1368.

50 A. Ahmadivand, B. Gerislioglu, Z. Ramezani and S. A. Ghoreishi, *Phys. Rev. Appl.*, 2019, **12**, 034018.

This journal is © the Owner Societies 2023

*Phys. Chem. Chem. Phys.*, 2023, **25**, 11375–11386 | 11385

51 N. Abhyankar, A. Agrawal, P. Shrestha, R. Maier, R. D. McMichael, J. Campbell and V. Szalai, *Sci. Adv.*, 2020, **6**, eabb0620.

52 X. Y. Liu, Z. Z. Liu, M. Hua, L. Y. Wang, W. W. Zhang, Y. F. Ning, Y. P. Shi and X. D. Wang, *ACS Appl. Nano Mater.*, 2020, **3**, 2129–2133.

53 K. Naito, Y. Kagawa, S. Utsuno, T. Naganuma and K. Kurihara, *Compos. Sci. Technol.*, 2009, **69**, 2027–2029.

54 A. A. Basharin, V. Chuguevsky, N. Volsky, M. Kafesaki and E. N. Economou, *Phys. Rev. B*, 2017, **95**, 035104.

55 M. Kuttge, G. Javier and A. Polman, *Nano Lett.*, 2010, **10**, 1537–1541.

56 J. A. Smith, C. Clear, K. C. Balram, D. P. S. McCutcheon and J. G. Rarity, *Phys. Rev. Appl.*, 2021, **15**, 034029.

57 C. Wang, Y. F. Li, M. C. Feng, J. F. Wang, H. Ma, J. Q. Zhang and S. B. Qu, *J. Phys. D: Appl. Phys.*, 2019, **52**, 155103.

58 M. Rahmanzadeh, M. Rajabalipanah and A. Abdolali, *Appl. Opt.*, 2018, **57**, 959–968.

59 C. R. Williams, S. R. Andrews, S. A. Maier, A. I. FernándezDomínguez, L. Martín-Moreno and F. J. García-Vidal, *Nat. Photonics*, 2008, **2**, 175–179.

60 Z. Li, L. Liu, H. Sun, Y. Sun, C. Gu, X. Chen, Y. Liu and Y. Luo, *Phys. Rev. Appl.*, 2017, **7**, 044028.

61 W. L. Guo, G. M. Wang, K. Chen, H. P. Li, Y. Q. Zhuang and H. X. Xu, *Phys. Rev. Appl.*, 2019, **12**, 014009.

62 J. F. Zhu, Z. F. Ma, W. J. Sun, F. Ding, Q. He, L. Zhou and Y. G. Ma, *Appl. Phys. Lett.*, 2014, **105**, 021102.

63 D. R. Smith, D. C. Vier, T. Koschny and C. M. Soukoulis, *Phys. Rev. E: Stat., Nonlinear, Soft Matter Phys.*, 2005, **71**, 036617.

64 H. Xiong and Q. Shen, *Nanoscale*, 2020, **12**, 14598.

65 M. A. Hernández-Acosta, L. Soto-Ruvalcaba, C. L. Martínez-González, M. Trejo-Valdez and C. Torres-Torres, *Phys. Scr.*, 2019, **94**, 125802.